Eurographics/ ACM SIGGRAPH Symposium on Computer Animation (2012)
P. Kry and J. Lee (Editors)

Energetically Consistent Invertible Elasticity

Alexey Stomakhin[†1], Russell Howes[‡1], Craig Schroeder[§1] and Joseph M. Teran[¶1]

[1]Department of Mathematics, University of California, Los Angeles, USA

Abstract

We provide a smooth extension of arbitrary isotropic hyperelastic energy density functions to inverted configurations. This extension is designed to improve robustness for elasticity simulations with extremely large deformations and is analogous to the extension given to the first Piola-Kirchoff stress in [ITF04]. We show that our energy-based approach is significantly more robust to large deformations than the first Piola-Kirchoff fix. Furthermore, we show that the robustness and stability of a hyperelastic model can be predicted from a characteristic contour, which we call its primary contour. The extension to inverted configurations is defined via extrapolation from a convex threshold surface that lies in the uninverted portion of the principal stretches space. The extended hyperelastic energy density yields continuous stress and unambiguous stress derivatives in all inverted configurations, unlike in [TSIF05]. We show that our invertible energy-density-based approach outperforms the popular hyperelastic corotated model, and we also show how to use the primary contour methodology to improve the robustness of this model to large deformations.

Categories and Subject Descriptors (according to ACM CCS): I.3.5 [Computer Graphics]: Computational Geometry and Object Modeling—Physically based modeling

1. Introduction

Large strain deformable object simulation was introduced to computer graphics by [TPBF87]. Simulation of such phenomena is now an indispensable tool for creating realistic virtual environments [BZ11, KJ09, FGBP11]. Unfortunately, the simulation of such large deformation problems with a Lagrangian mesh is notoriously unstable and error-prone. Although many researchers have shown the effectiveness of adaptive refinement [SPB00, DDCB01, GKPS02, CGDP04] and hybrid Lagrangian/Eulerian approaches [BWHT07, WTGT09, WT08, WRK*10], computer graphics researchers tend to use purely Lagrangian methods with a topologically static mesh. The primary problem for Lagrangian methods is the inversion of mesh elements that poorly approximate highly deformed regions. This motivated the development of models that are well defined when the deformation mapping has negative Jacobian. Irving et al. developed the invertible finite element (IFE) framework in [ITF04] and [TSIF05] to extend arbitrary elastic constitutive models to inverted configurations. The "warped stiffness" [MDM*02, ST08, ZSTB10, MG04, EKS03] and corotated hyperelasticity [CPSS10, MZS*11] models are also meaningfully defined through inversion. Another notable model defined through inversion was developed in [THMG04].

We build on the IFE framework in [ITF04] and [TSIF05] to provide a method for the practical extension of an arbitrary isotropic hyperelastic energy density to inverted configurations. Hyperelasticity refers to constitutive models for which the stress is determined as the gradient of an underlying scalar energy density. Our extension matches the original model for singular values on the uninverted side of a convex extrapolation threshold surface. In fact, we provide a heuristic that prevents the need for the costly SVD whenever the material is in this uninverted region. The smoothly extended energy allows for accurate and unambiguous definition of the stress and stress derivatives needed for force computation and implicit time integration. We show that this extension provides significantly superior behavior through inversion than both the original IFE and the corotated models in [CPSS10] and [MZS*11]. Lastly, we also show that

† e-mail: alexey@math.ucla.edu
‡ e-mail: rhowes@math.ucla.edu
§ e-mail: craig@math.ucla.edu
¶ e-mail: jteran@math.ucla.edu

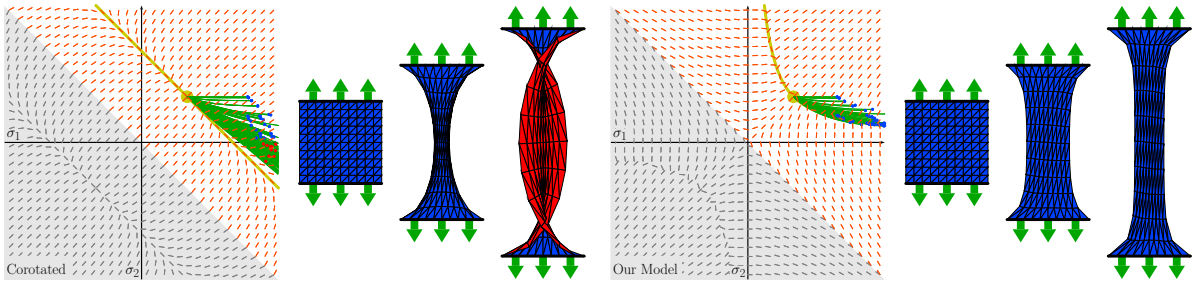

Figure 1: *A 2D mattress is stretched by two sides and the evolution of its elements is shown in the principal stretches space. The arrows (orange) show the downhill direction of the energy gradient. The gray region is invalid in accordance with the IFE convention [ITF04]. The green curves show singular value trajectories from the undeformed configuration* $(1,1)$ *(yellow dot) to the final configuration (colored dots) for each element in the mesh as it is stretched. The trajectories tend to follow the primary contour (yellow). The corotated model primary contour crosses the axes, leading to nonphysical inversion (red) for sufficiently large stretches.*

our new notion of a primary contour provides useful analysis of a model's robustness to large deformation.

2. Isotropic hyperelasticity

We limit our discussion of elasticity to the constitutive stress/strain relationship. We provide enough detail that any spatial or temporal discretization technique can be used in practice. Specifically, we will describe how to compute stress needed for elastic forces and stress linearizations needed for implicit time stepping. Note that our energy-based approach works naturally with variational integrators like those in [KYT*06].

We assume a continuum description of the deformation $\boldsymbol{\phi} : \Omega_0 \rightarrow \mathbb{R}^3$ that maps initial (or material) points $\boldsymbol{X}$ in the initial configuration Ω_0 to points $\boldsymbol{x} = \boldsymbol{\phi}(\boldsymbol{X})$ in world space. The elastic force per unit volume in the continuum body is $\nabla^{\boldsymbol{X}} \cdot \boldsymbol{P}$, where $\boldsymbol{P}$ is the first Piola-Kirchoff stress [GS08]. For hyperelasticity, the first Piola-Kirchoff stress is determined from the energy density $\Psi(\boldsymbol{F})$ as $\boldsymbol{P} = \frac{\partial \Psi}{\partial \boldsymbol{F}}$, where $\boldsymbol{F} = \frac{\partial \boldsymbol{\phi}}{\partial \boldsymbol{X}}$ is the deformation gradient. We limit our focus to isotropic models for which the energy density can be written as $\Psi(\boldsymbol{F}) = \hat{\Psi}(\boldsymbol{\sigma})$, where $\boldsymbol{F} = \boldsymbol{U}\boldsymbol{\Sigma}\boldsymbol{V}^T$ and $\boldsymbol{\sigma} = \text{diag}(\boldsymbol{\Sigma}) = (\sigma_1, \sigma_2, \sigma_3)$. Note that isotropy is equivalent to defining the energy in terms of $I_1 = \sigma_1^2 + \sigma_2^2 + \sigma_3^2$, $I_2 = \sigma_1^2\sigma_2^2 + \sigma_2^2\sigma_3^2 + \sigma_1^2\sigma_3^2$, and $J = \sigma_1\sigma_2\sigma_3$ [GS08]. This implies that the energy is invariant under permutations of the singular values. In this case, it can be shown that the first Piola-Kirchoff stress has the form $\boldsymbol{P}(\boldsymbol{F}) = \boldsymbol{U}\hat{\boldsymbol{P}}(\boldsymbol{\sigma})\boldsymbol{V}^T$ where

$$\hat{\boldsymbol{P}}(\boldsymbol{\sigma}) = \begin{bmatrix} \hat{P}_1(\boldsymbol{\sigma}) & & \\ & \hat{P}_2(\boldsymbol{\sigma}) & \\ & & \hat{P}_3(\boldsymbol{\sigma}) \end{bmatrix}$$

with $\hat{P}_i = \hat{\Psi}_{\sigma_i} = \frac{\partial \hat{\Psi}}{\partial \sigma_i}$. Furthermore, the linearization of the stress around a given $\boldsymbol{F}$ is $\delta\boldsymbol{P} = \frac{\partial \boldsymbol{P}}{\partial \boldsymbol{F}}(\boldsymbol{F}) : \delta\boldsymbol{F}$ and in the case of isotropy, this can be shown to satisfy $\delta\boldsymbol{P} = \boldsymbol{U}\left(\frac{\partial \boldsymbol{P}}{\partial \boldsymbol{F}}(\boldsymbol{\Sigma}) : \left(\boldsymbol{U}^T\delta\boldsymbol{F}\boldsymbol{V}\right)\right)\boldsymbol{V}^T$. Although the term $\frac{\partial \boldsymbol{P}}{\partial \boldsymbol{F}}(\boldsymbol{\Sigma})$ was shown to have a block diagonal structure in terms of the invariants of $\boldsymbol{F}$ in [TSIF05], we prefer to express this block structure in terms of the principal stretches as in [SZL*11]. If we reorder the $3 \times 3 \times 3 \times 3$ fourth order tensor $\frac{\partial \boldsymbol{P}}{\partial \boldsymbol{F}}(\boldsymbol{\Sigma})$ as a 9×9 matrix using the convention that a 3×3 matrix $\boldsymbol{S}$ is reordered as a 9-vector with components $(s_{11}, s_{22}, s_{33}, s_{12}, s_{21}, s_{13}, s_{31}, s_{23}, s_{32})$, then $\frac{\partial \boldsymbol{P}}{\partial \boldsymbol{F}}(\boldsymbol{\Sigma})$ can be shown (see supplementary document) to have the four diagonal blocks $\boldsymbol{A}$, $\boldsymbol{B}_{12}$, $\boldsymbol{B}_{13}$ and $\boldsymbol{B}_{23}$ with

$$\boldsymbol{A} = \begin{bmatrix} \hat{\Psi}_{\sigma_1\sigma_1} & \hat{\Psi}_{\sigma_1\sigma_2} & \hat{\Psi}_{\sigma_1\sigma_3} \\ \hat{\Psi}_{\sigma_2\sigma_1} & \hat{\Psi}_{\sigma_2\sigma_2} & \hat{\Psi}_{\sigma_2\sigma_3} \\ \hat{\Psi}_{\sigma_3\sigma_1} & \hat{\Psi}_{\sigma_3\sigma_2} & \hat{\Psi}_{\sigma_3\sigma_3} \end{bmatrix}$$

and

$$\boldsymbol{B}_{ij} = \frac{1}{\sigma_i^2 - \sigma_j^2} \begin{bmatrix} \sigma_i\hat{\Psi}_{\sigma_i} - \sigma_j\hat{\Psi}_{\sigma_j} & \sigma_j\hat{\Psi}_{\sigma_i} - \sigma_i\hat{\Psi}_{\sigma_j} \\ \sigma_j\hat{\Psi}_{\sigma_i} - \sigma_i\hat{\Psi}_{\sigma_j} & \sigma_i\hat{\Psi}_{\sigma_i} - \sigma_j\hat{\Psi}_{\sigma_j} \end{bmatrix}.$$

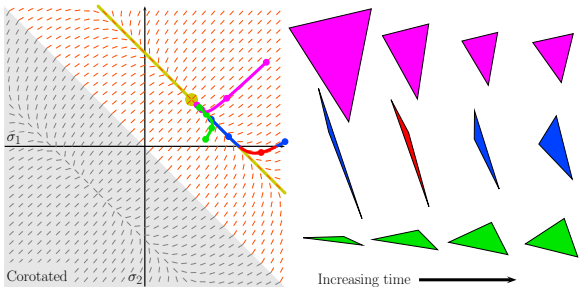

Figure 2: *Three triangles are allowed to relax from different initially deformed configurations. Their trajectories in singular value space are shown with corresponding colors on the left. Note the strong attraction to the primary contour (yellow) causes the blue triangle to invert (shown in red).*

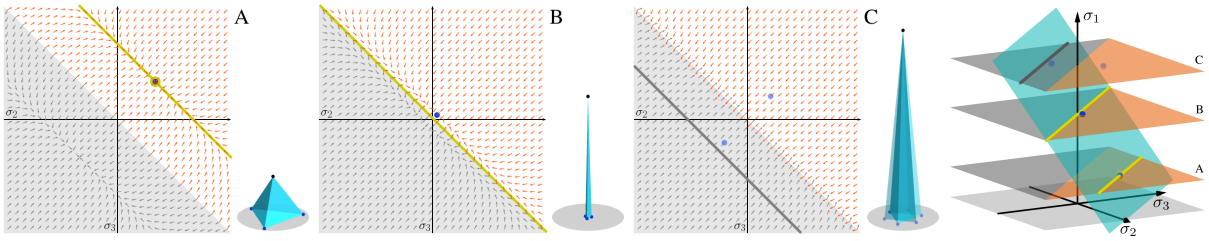

Figure 3: *We stretch a tetrahedron with its base fixed to a plane. The plots show the corotated energy gradients in constraint planes of increasing σ_1. The equilibrium singular values are shown in blue. The yellow line is the intersection of the constraint plane with the primary contour. As the tetrahedron is stretched, the line shifts. The primary contour does not intersect the third slice, but we show in dark gray where it would intersect if it were extended into the invalid region (gray). The primary contour draws the configuration into a minimum at the energy kink, leading to nonphysical oscillation. For illustrative purposes we slightly abused the IFE convention on the constraint plane C to demonstrate how the configuration is driven towards the kink, although in fact it never can get to the invalid region and keeps "bouncing back."*

As in [SZL*11], care must be taken to robustly treat the possibly small denominators in the components of $\boldsymbol{B}_{ij}$. These expressions for the stress and stress derivatives are used to compute forces and their linearizations directly from our extended hyperelastic energy densities in all configurations (inverted or otherwise). As in [TSIF05], the one 3×3 and three 2×2 matrices can be readily projected to their nearest SPD counterpart to guarantee that conjugate gradient can reliably be used for solving the discrete systems that arise with implicit time stepping.

3. Invertible hyperelastic energy densities

We propose the invertible extension of $\hat{\Psi}$, rather than the extension of its derivatives $\hat{\boldsymbol{P}}$ as was originally advocated in [ITF04]. That is, these functions are extended to the portion of singular value space where singular values can be negative. In general, an extension of $\hat{\boldsymbol{P}}$ is not guaranteed to be consistent with a hyperelastic strain energy density, and the procedural modification complicates the definition of stress derivatives needed with implicit time stepping. In fact, [TSIF05] were forced to evaluate stress derivatives in a nearby uninverted configuration which lead to inconsistency between the stress and its derivatives. We will show that an energetic extension of the constitutive model is far more simplistic, robust and stable than the original stress based extension. However, we first discuss some fundamental properties of hyperelastic energy densities defined over the inverted portion of singular value space.

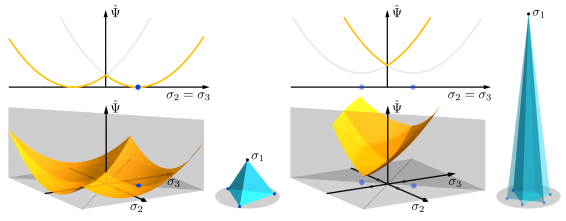

Figure 4: *We plot the energy surface $\hat{\Psi}(c, \sigma_2, \sigma_3)$ for the example in Figure 3 for $c = 1$ (left) and $c = 5$ (right). The plots on top show the energy profile along the line $\sigma_2 = \sigma_3$, which is orthogonal to the kink at $\sigma_2 + \sigma_3 = 0$. The blue dots show the quasistatic solutions that would be obtained assuming a smooth energy profile. In the image at the left, the minimizer is away from the energy kink. However, as the top vertex is stretched the minimum approaches the kink which leads to non-physical oscillations. For illustrative purposes we slightly abused the IFE convention on the right side as in Figure 3.*

3.1. Energy kinks

As previously mentioned, isotropy implies that the energy density $\hat{\Psi}$ is invariant under permutations of the singular values. Isotropy is only one source of symmetry in models defined over inverted configurations.

Standard SVD convention dictates that singular values are always nonnegative. However, in order for the $\boldsymbol{U}$ and $\boldsymbol{V}$ matrices to correspond to rotations some singular values might need to be negated. This brings in non-uniqueness in the sense that we are free to choose which singular values get the negative sign. We resolve this with the IFE convention [ITF04] and negate, if needed, the one with the smallest magnitude. As a result, the combinations of singular values that do not obey this convention cannot possibly occur. They form an *invalid region* in the principal stretch space, which we show in gray in Figures 1, 2 and 3. Although such combinations will never be computed, we can consider the energy density as being defined over these

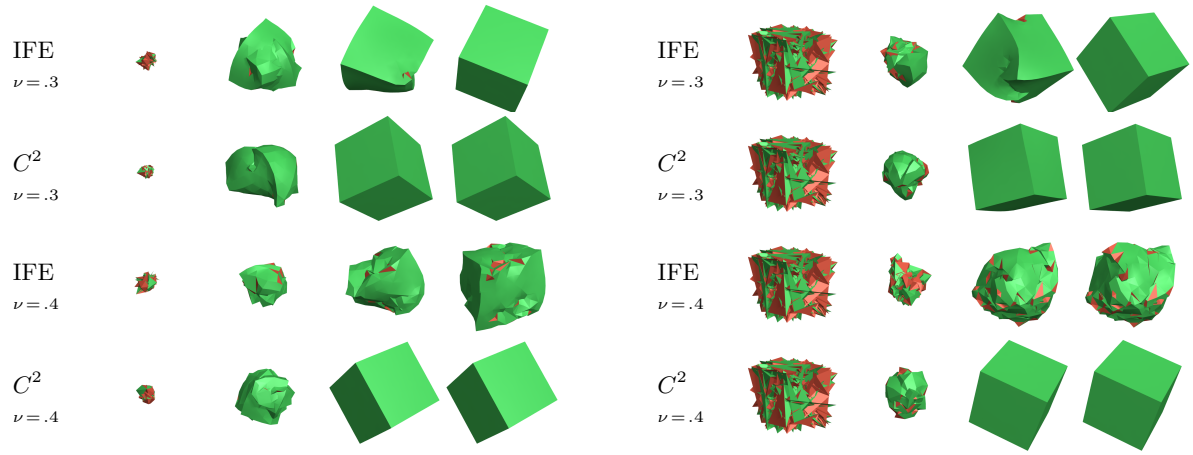

Figure 5: *In these stress tests we initially perturb the vertices of a cube mesh to a point (left) or randomly (right) and allow it to recover. Our model resolves itself for a wide range of Lamé coefficients, while a typical IFE implementation fails to recover for large Poisson's ratios (ν).*

excluded combinations by ensuring that combinations corresponding to the same deformation gradient are assigned the same energy densities. This enforces invariance under pairs of singular value sign flips and results in a second form of symmetry.

The aforementioned symmetries can lead to a kink in the energy density. For example in 2D if we negate the singular values σ_1 and σ_2, then we must have $\hat{\Psi}(\sigma_1, \sigma_2) = \hat{\Psi}(-\sigma_1, -\sigma_2)$ since these configurations correspond to the same deformation gradient. Furthermore, if we then permute these values we must have $\hat{\Psi}(\sigma_1, \sigma_2) = \hat{\Psi}(-\sigma_2, -\sigma_1)$. Consider the energy along the line $\sigma_1(t) = s + t$ and $\sigma_2(t) = -s + t$, where s is arbitrary, but fixed. Then, $\psi(t) = \hat{\Psi}(s + t, -s + t) = \hat{\Psi}(s - t, -s - t) = \psi(-t)$. Then, either $\psi'(0) = 0$ or $\psi(t)$ has a kink at $t = 0$.

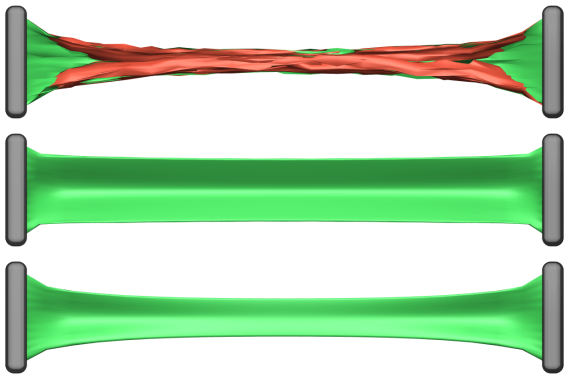

Figure 6: *Comparison of our C^2 Neo-Hookean-based model (bottom) with corotational elasticity (top) and corotational with our fix (middle). The corotational model is unstable under these stretched configurations, and many inverted elements arise (shown in red). Our fix to the corotational model prevents the instability and inversion but does not look as realistic (the cross section resembes an X) as our C^2 model. Note that unmodified Neo-Hookean will produce the same result as our extension, since the extrapolation threshold was not reached in this example.*

Note that $\psi'(0)$ is the component of the stress orthogonal to the line $\sigma_1 + \sigma_2 = 0$ at the point $(s, -s)$. Therefore, any energy density that leads to a nonzero orthogonal stress contribution at the line $\sigma_1 + \sigma_2 = 0$ must have a kink there. Since the orthogonal stress component is required to leave this line, a kink in the energy density profile is actually desirable. Otherwise, the model would be inherently compliant to inversion with a weak restoring force near this line. Note that energy densities defined in terms of the invariants tend not to produce such a kink. Indeed, consider an energy defined in terms of the invariants $\hat{\Psi}(\sigma_1, \sigma_2) = \tilde{\Psi}(I_1, J) = \tilde{\Psi}(\sigma_1^2 + \sigma_2^2, \sigma_1\sigma_2)$. The component of the stress orthogonal to the line $\sigma_1 + \sigma_2 = 0$ is given as $\hat{\Psi}_{\sigma_1} + \hat{\Psi}_{\sigma_2}$. We can then see from the invariants that $\hat{\Psi}_{\sigma_1} + \hat{\Psi}_{\sigma_2} = (2\sigma_1\tilde{\Psi}_{I_1} + \sigma_2\tilde{\Psi}_{I_2}) + (2\sigma_2\tilde{\Psi}_{I_1} + \sigma_1\tilde{\Psi}_{I_2}) = (\sigma_1 + \sigma_2)(2\tilde{\Psi}_{I_1} + \tilde{\Psi}_{I_2}) = 0$ when $\sigma_1 + \sigma_2 = 0$, provided the partials in the invariants remain bounded. The situation is analogous in 3D with the kink arising along the plane $\sigma_2 + \sigma_3 = 0$. See Figures 4 and 8 (right) for visualizations of the kinks.

We will show that despite the fact that the kink arises only at the boundary of the valid region, it still plays a fundamental role in the behavior of the model.

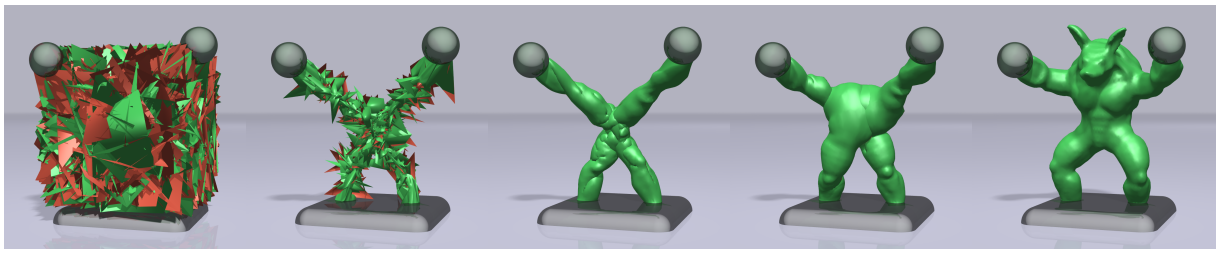

Figure 7: *We randomly scatter the vertices of an armadillo mesh and let it relax to rest. Our energy based approach robustly handles extremely large deformations with many severely deformed and inverted elements (shown in red).*

3.2. Primary contour

Hyperelastic constitutive models are characterized by a strongly attractive basin which we call the *primary contour* of the model. For example, a model with Poisson's ratio very close to $\frac{1}{2}$ may be more strongly attracted to the submanifold corresponding to volume preservation than to the rest configuration. Let $\boldsymbol{v}$ be the eigenvector of the energy Hessian $H_{ij} = \frac{\partial^2 \hat{\Psi}}{\partial \sigma_i \partial \sigma_j}$ with the largest-magnitude eigenvalue, and let $g_i = \frac{\partial \hat{\Psi}}{\partial \sigma_i}$ be the energy gradient. We define the primary contour to be the region where $\boldsymbol{v} \cdot \boldsymbol{g} = 0$. The Hessian describes how $\boldsymbol{g}$ changes, and $\boldsymbol{v}$ describes the direction of greatest change of $\boldsymbol{g}$. Thus, as the configuration moves from the primary contour, the $\boldsymbol{v}$ component of $\boldsymbol{g}$ will dominate. This tends to draw the configuration towards the primary contour. When it gets close, the $\boldsymbol{v}$ component diminishes, and the configuration moves mostly along the contour. This phenomenon is shown in Figures 1 and 2. Problems arise when the contour crosses over into the inverted regime or when it approaches a kink in the energy.

Failure to define a model with an appropriate primary contour can lead to catastrophic behavior, which we demonstrate in the following section.

3.3. Corotational hyperelasticity

Models designed to correct the rotational artifacts inherent in linear elasticity are very popular in computer graphics [MDM*02, ST08, ZSTB10, MG04, EKS03]. The hyperelastic version is detailed in [CPSS10] and [MZS*11]. The corotated model takes the form

$$\hat{\Psi} = \mu \sum_i (\sigma_i - 1)^2 + \frac{\lambda}{2}\Big(\sum_i (\sigma_i - 1)\Big)^2.$$

The gradient is $g_i = 2\mu(\sigma_i - 1) + \lambda \sum_j (\sigma_j - 1)$, and the Hessian is $H_{ij} = 2\mu\delta_{ij} + \lambda$. Its largest eigenvector is $v_i = 1$ with eigenvalue $2\mu + d\lambda$, where d is the dimension. The other eigenvalues are 2μ with eigenvectors orthogonal to $\boldsymbol{v}$. Finally, $\boldsymbol{v} \cdot \boldsymbol{g} = 0$ implies $\sum_i (\sigma_i - 1) = 0$ is the equation for the primary contour. Note that this primary contour crosses into the inverted region.

Consider the 2D examples shown in Figure 2, which shows material relaxation from three distinct initial configurations. Note that all three trajectories initially tend towards the primary contour. Unfortunately, the trajectory highlighted in blue passes through the inverted region on its way to the primary contour. This behavior is also observed on a macroscopic scale and under mesh refinement, as shown in Figure 1.

The corotated primary contour is also problematic because it intersects the kink in the energy density. Consider the behavior of the single tetrahedron shown in Figure 3 as it undergoes a stretching deformation. The intersection of the primary contour and the plane $\sigma_1 = c$ is shown at different stages. Note that the relevant slice of the primary contour eventually drives the configuration towards the invalid state that violates the sign convention. This ultimately leads to an energy minimum that lies on a kink, as shown in Figure 4. The discontinuity of the stress at this minimum causes nonphysical oscillations, the problematic consequences of which are shown on a macroscopic scale in Figure 6.

3.4. Corotational correction

Note that the corotated primary contour is determined primarily by the λ term. Further, the corrective behavior of the corotated model can largely be attributed to its μ term. This suggests that a more suitable model can be constructed by replacing the λ term with one that leads to a more favorable primary contour. One such model is

$$\hat{\Psi} = \mu \sum_i (\sigma_i - 1)^2 + \frac{\lambda}{2}(J - 1)^2.$$

Similar λ terms were used in [Ogd98, THMG04]. This model has the primary contour $J = 1$, which does not intersect the inverted region. While the model still has limitations, it fixes the stretching problems of the corotated model (see Figure 6).

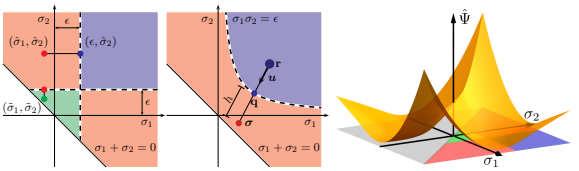

Figure 8: *The leftmost images show the relevant regions in the 2D C^1 and C^2 extensions respectively. The C^1 $\hat{\Psi}^{ext}$ is shown at the right. Note the kink discussed in Section 3.1 along the line $\sigma_1 + \sigma_2 = 0$. The C^2 $\hat{\Psi}^{ext}$ looks similar.*

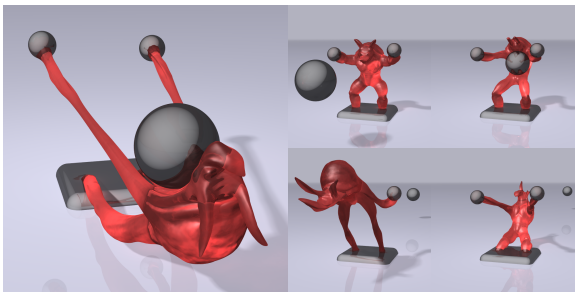

Figure 9: ***"Ouch."*** *An armadillo is hit with a ball.*

4. Energy extrapolation

We provide both C^1 and C^2 extensions to arbitrary isotropic energy densities $\hat{\Psi}$. We show that these extensions can produce models with well-behaved primary contours. The C^1 extension is easier to implement and results in continuous stresses but discontinuous stress derivatives. The C^2 extension has continuous stress and stress derivatives and provides added robustness in some scenarios. Our extension to $\hat{\Psi}$ is accomplished by polynomial extrapolation from a convex contour in the uninverted portion of singular value space that increases the energy density as the configuration inverts. We present only the energy densities below; see the supplementary document for derivatives and more details.

4.1. C^1 extension

We define the C^1 extended energy density $\hat{\Psi}^{\text{ext}}$ to coincide with the original $\hat{\Psi}$ whenever the singular values are all above a threshold ϵ. This region is illustrated in blue in the left image of Figure 8 for a 2D problem. If one singular value σ_i is less than this threshold (region shown in red), then we extend the energy quadratically in the direction σ_i from the closest point in the blue region. Consider the point $(\hat{\sigma}_1, \hat{\sigma}_2)$ in Figure 8. In this case, only $\hat{\sigma}_1$ is below ϵ, and the extension is given as $\hat{\Psi}^{\text{ext}}(\hat{\sigma}_1, \hat{\sigma}_2) = \hat{\Psi}(\epsilon, \hat{\sigma}_2) + \hat{\Psi}_{\sigma_1}(\epsilon, \hat{\sigma}_2)[\hat{\sigma}_1 - \epsilon] + \frac{k}{2}[\hat{\sigma}_1 - \epsilon]^2$. This extension will be C^1 as we transition from the blue region to the red region for all values of the parameter k. This parameter is used to add extra resistance to inversion but does not degrade the C^1 regularity of the extension. For points $(\tilde{\sigma}_1, \tilde{\sigma}_2)$ with both principal stretches below the threshold we define another region (shown in green) and quadratically extend the energy from the nearest point in the red region. It does not matter which red region we extend from, since in both cases we have $\hat{\Psi}^{\text{ext}}(\tilde{\sigma}_1, \tilde{\sigma}_2) = \hat{\Psi}(\epsilon, \epsilon) + \hat{\Psi}_{\sigma_1}(\epsilon, \epsilon)[\hat{\sigma}_1 - \epsilon] + \hat{\Psi}_{\sigma_2}(\epsilon, \epsilon)[\hat{\sigma}_2 - \epsilon] + \hat{\Psi}_{\sigma_1\sigma_2}(\epsilon, \epsilon)[\hat{\sigma}_1 - \epsilon][\hat{\sigma}_2 - \epsilon] + \frac{k}{2}\left([\hat{\sigma}_1 - \epsilon]^2 + [\hat{\sigma}_2 - \epsilon]^2\right)$. The 3D extension is analogous but with an additional type of region. Note that we can avoid the SVD if $I_1/J^2 \geq \epsilon$ (2D) or $I_2/J^2 \geq \epsilon$ (3D), since these imply that $\sigma_i > \epsilon$.

4.2. C^2 extension

We use a different extrapolation surface for our C^2 model, since the one used in C^1 leads to an unfavorable primary contour when extended to C^2. We define the C^2 extension whenever the determinant of the deformation gradient (or product of singular values) is below a threshold ϵ. The base energy density $\hat{\Psi}$ is extended to the extrapolated $\hat{\Psi}^{\text{ext}}$ at a given point $\boldsymbol{\sigma} = (\sigma_1, \sigma_2, \sigma_3)$ by extrapolating along the line to the rest configuration point $\boldsymbol{r} = (1, 1, 1)$. Extrapolation begins at the intersection of the line and the contour surface $\sigma_1\sigma_2\sigma_3 = \epsilon$ and is chosen so that all first and second derivatives of the extended energy match those of $\hat{\Psi}$ at the intersection point (see Figure 8). This $\hat{\Psi}^{\text{ext}}$ gives continuous stress and stress derivatives, but it is complicated by the need for the value and derivative of the intersection point between the line connecting $\boldsymbol{\sigma}$ and the extrapolation contour $\sigma_1\sigma_2\sigma_3 = \epsilon$.

Let $\boldsymbol{u} = \frac{\boldsymbol{r} - \boldsymbol{\sigma}}{|\boldsymbol{r} - \boldsymbol{\sigma}|}$ be the direction from the point $\boldsymbol{\sigma}$ to the rest configuration point $\boldsymbol{r}$. Denote the intersection between the line and the threshold surface as $\boldsymbol{q} = \boldsymbol{r} + s(\boldsymbol{\sigma} - \boldsymbol{r})$, where the scalar s is given by the roots of the cubic equation $q_1 q_2 q_3 = \epsilon$. If we denote the distance from $\boldsymbol{\sigma}$ to $\boldsymbol{q}$ by h, then the extended energy has the form where we assume summation on repeated indices. The derivatives of the scalar s needed for stress and stress derivatives can be determined implicitly by differentiating the cubic equation $q_1 q_2 q_3 = \epsilon$.

$$\hat{\Psi}^{\text{ext}}(\boldsymbol{\sigma}) = \hat{\Psi}(\boldsymbol{q}) + h u_i \hat{\Psi}_{\sigma_i}(\boldsymbol{q}) + \frac{h^2}{2} u_i \hat{\Psi}_{\sigma_i \sigma_j}(\boldsymbol{q}) u_j$$

5. Examples

We demonstrate our extension methodology with a Neo-Hookean hyperelastic energy density

$$\hat{\Psi} = \frac{\mu}{2}\Big(\sum_i \sigma_i^2 - d\Big) - \mu \ln J + \frac{\lambda}{2}(\ln J)^2.$$

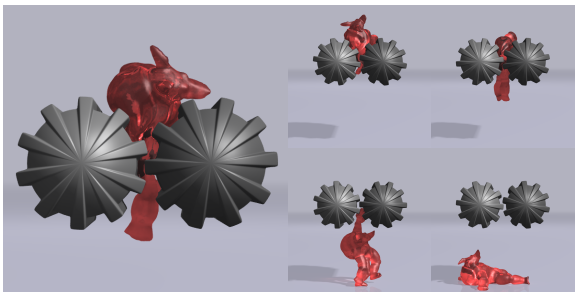

Figure 10: ***"Ouch again."*** *An armadillo is passed through gears.*

In Figures 9, 11, 12 and 13 we show examples run with the C^1 extension using an inversion threshold $\epsilon = 0.4$ and $k = 20 \times E$ where E is the Young's modulus. In general, smaller values of ϵ and larger values of k will increase resistance to extreme compression. In Figures 6, 7 and 10 we show examples run with our C^2 extension with threshold surface $J = \epsilon$ with $\epsilon = 0.9$. As with C^1, smaller values of ϵ increase resistance to extreme compression. Although $\epsilon = 0.9$ is somewhat large, smaller values of ϵ resulted in unnecessarily stiff response to compression due to the high energy barrier of the underlying Neo-Hookean constitutive model. Simulation statistics are shown below.

Fig	$\Delta t_{ave}(s)$	$\Delta x_{min}(m)$	Fig	$\Delta t_{ave}(s)$	$\Delta x_{min}(m)$
7	0.00043	0.0042	11	0.0015	0.010
9	0.00060	0.0042	12	0.00087	0.041
10	0.00036	0.0031	13	0.00011	0.0010

5.1. Comparison with IFE

Figure 5 shows a comparison of our C^2 model with IFE using implicit time integration on two common stress tests. In each case, our model performed significantly better with the same Lamé parameters. The IFE extension of the first Piola-Kirchoff stress used the same threshold contour with linear stress extrapolation and derivative clamping as in [ITF04, TSIF05]. Figure 1 (right) shows the primary contour for the 2D equivalent of our C^2 model. Note that the contour never extends into the inverted region. Furthermore the figure shows that the curve is a good predictor of the average trajectory of an element in the mesh. Because IFE lacks an energy in the extrapolated region, its primary contour cannot be used to predict its behavior there. These results suggest that our hyperelastic extension methodology allows us to readily design constitutive models that are more robust to extremely large deformation.

5.2. Comparison with corotated

The primary contours for our model and for corotational elasticity are shown in Figure 1. Notice that the corotational elasticity primary contour intersects the inverted region and ours does not. This feature prevents the tendency towards inverted equilibrium configurations and it also prevents instabilities that arise when the model drives the configuration towards the energy kink. Figure 6 illustrates the consequences of this behavior in a large scale example in 3D. The corotated model is driven towards the inverted region and to unstable minima at the energy kink. This leads to non-physical oscillation and inversion (shown in red). This behavior is prevented with our fix to the λ term in the corotational mode, however it still does not look as realistic as our Neo-Hookean-based extension.

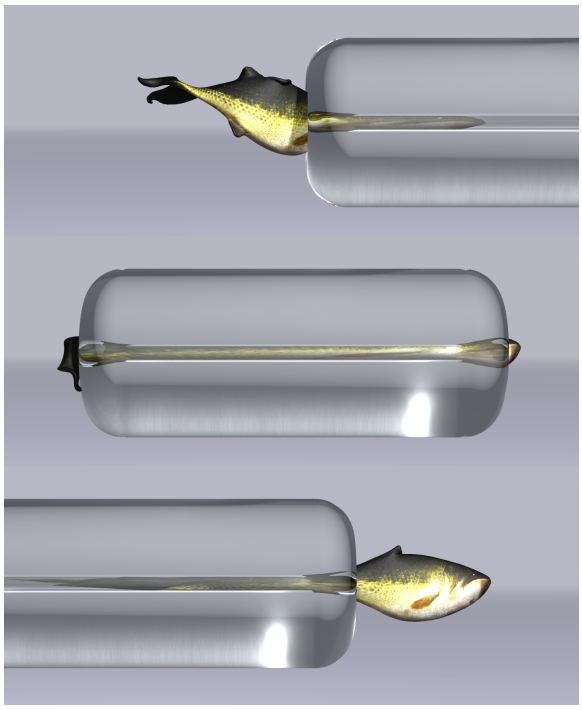

Figure 11: ***"Tight spaces."*** *A fish passing through a thin tube.*

References

[BWHT07] Bargteil A., Wojtan C., Hodgins J., Turk G.: A finite element method for animating large viscoplastic flow. *ACM Trans. Graph. 26* (2007). 1

[BZ11] Barbič J., Zhao Y.: Real-time large-deformation substructuring. *ACM Trans. Graph. 30* (2011), 91:1–91:8. 1

[CGDP04] Capell S., Green S., Duchamp B., Popovic Z.: A multiresolution framework for dynamics deformations. In *Proc. Symp. Comp. Anim.* (2004), pp. 131–140. 1

[CPSS10] Chao I., Pinkall U., Sanan P., Schröder P.: A simple geometric model for elastic deformations. *ACM Trans. Graph. 29* (2010), 38:1–38:6. 1, 5

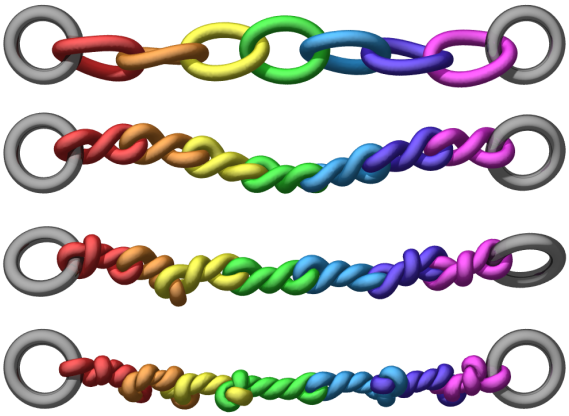

Figure 12: ***"That's twisted."*** *7 elastic links in a braiding example.*

Figure 13: ***"Yummy."*** *25 gelatin cubes falling in a bowl.*

[DDCB01] Debunne G., Desbrun M., Cani M., Barr A.: Dynamic real-time deformations using space and time adaptive sampling. In *Proc. SIGGRAPH* (2001), pp. 31–36. 1

[EKS03] Etzmuss O., Keckeisen M., Strasser W.: A fast finite element solution for cloth modeling. In *Proc. Pac. Graph.* (2003), pp. 244–251. 1, 5

[FGBP11] Faure F., Gilles B., Bousquet G., Pai D.: Sparse meshless models of complex deformable solids. *ACM Trans. Graph. 30* (2011). 1

[GKPS02] Grinspun E., Krysl P., P. Schröder P.: Charms: a simple framework for adaptive simulation. *ACM Trans. Graph. 21* (2002), 281–290. 1

[GS08] Gonzalez O., Stuart A.: *A first course in continuum mechanics.* Cambridge Texts in Applied Mathematics, 2008. 2

[ITF04] Irving G., Teran J., Fedkiw R.: Invertible finite elements for robust simulation of large deformation. In *Proc. Symp. Comp. Anim.* (2004), pp. 131–140. 1, 2, 3, 7

[KJ09] Kim T., James D.: Skipping steps in deformable simulation with online model reduction. *ACM Trans. Graph. 28* (2009). 1

[KYT*06] Kharevych L., Yang W., Tong Y., Kanso E., Marsden J., Schröder P.: Geometric, variational integrators for computer animation. In *Proc. Symp. Comp. Anim.* (2006), pp. 43–51. 2

[MDM*02] Müller M., Dorsey J., McMillan L., Jagnow R., Cutler B.: Stable real-time deformations. In *Proc. Symp. Comp. Anim.* (2002), pp. 49–54. 1, 5

[MG04] Müller M., Gross M.: Interactive virtual materials. In *Proc. Graph. Int.* (2004), pp. 239–246. 1, 5

[MZS*11] McAdams A., Zhu Y., Selle A., Empey M., Tamstorf R., Teran J., Sifakis E.: Efficient elasticity for character skinning with contact and collisions. *ACM Trans. Graph. 30* (2011), 37:1–37:12. 1, 5

[Ogd98] Ogden W.: *Nonlinear Elastic Deformations.* Dover, 1998. 5

[SPB00] Shamir A., Pascucci V., Bajaj C.: Multiresolution dynamic meshes with arbitrary deformations. In *Proc. IEEE Vis.* (2000), pp. 423–430. 1

[ST08] Schmedding R., Teschner M.: Inversion handling for stable deformable modeling. *Vis. Comp. 24* (2008), 625–633. 1, 5

[SZL*11] Sin F., Zhu Y., Li Y., Schroeder D., Barbic J.: Invertible isotropic hyperelasticity using svd gradients. In *Poster: Symp. Comp. Anim.* (2011), pp. 1–2. 2

[THMG04] Teschner M., Heidelberger B., Müller M., Gross M.: A versatile and robust model for geometrically complex deformable solids. In *Proc. Comp. Graph. Int.* (2004), pp. 312–319. 1, 5

[TPBF87] Terzopoulos D., Platt J., Barr A., Fleischer K.: Elastically deformable models. *ACM SIGGRAPH 21* (1987), 205–214. 1

[TSIF05] Teran J., Sifakis E., Irving G., Fedkiw R.: Robust quasistatic finite elements and flesh simulation. In *Proc. Symp. Comp. Anim.* (2005), pp. 181–190. 1, 2, 3, 7

[WRK*10] Wicke M., Ritchie D., Klingner B., Burke S., Shewchuk J., O'Brien J.: Dynamic local remeshing for elastoplastic simulation. *ACM Trans. Graph. 29* (2010), 49:1–49:11. 1

[WT08] Wojtan C., Turk G.: Fast viscoelastic behavior with thin features. *ACM Trans. Graph. 27* (2008), 47:1–47:8. 1

[WTGT09] Wojtan C., Thürey N., Gross M., Turk G.: Deforming meshes that split and merge. *ACM Trans. Graph. 28* (2009), 76:1–76:10. 1

[ZSTB10] Zhu Y., Sifakis E., Teran J., Brandt A.: An efficient and parallelizable multigrid framework for the simulation of elastic solids. *ACM Trans. Graph. 29* (2010), 16:1–16:18. 1, 5